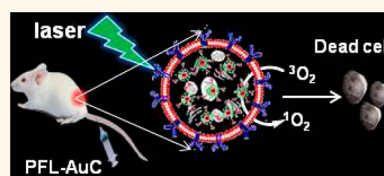# Fluorescence Imaging Assisted Photodynamic Therapy Using Photosensitizer-Linked Gold Quantum Clusters

Lakshmi V. Nair,[†] Shaiju S. Nazeer,[†] Ramapurath S. Jayasree,*,[†] and Ayyappanpillai Ajayaghosh*,[‡]

[†]Biophotonics and Imaging Laboratory, Bio Medical Technology Wing, Sree Chitra Tirunal Institute for Medical Sciences and Technology (SCTIMST), Trivandrum 695012, India and [‡]Photosciences and Photonics Group, Chemical Sciences and Technology Division, CSIR-National Institute for Interdisciplinary Science and Technology (CSIR-NIIST), Trivandrum 695019, India

ABSTRACT Fluorescence imaging assisted photodynamic therapy (PDT) is a viable two-in-one clinical tool for cancer treatment and follow-up. While the surface plasmon effect of gold nanorods and nanoparticles has been effective for cancer therapy, their emission properties when compared to gold nanoclusters are weak for fluorescence imaging guided PDT. In order to address the above issues, we have synthesized a near-infrared-emitting gold quantum cluster capped with lipoic acid (L-AuC with $(Au)_{18}(L)_{14}$) based nanoplatform with excellent tumor reduction property by incorporating a tumor-targeting agent (folic acid) and a photosensitizer (protoporphyrin IX), for selective PDT. The synthesized quantum cluster based photosensitizer PFL-AuC showed 80% triplet quantum yield when compared to that of the photosensitizer alone (63%). PFL-AuC having 60 μg (0.136 mM) of protoporphyrin IX was sufficient to kill 50% of the tumor cell population. Effective destruction of tumor cells was evident from the histopathology and fluorescence imaging, which confirm the *in vivo* PDT efficacy of PFL-AuC.

KEYWORDS: gold quantum cluster · photodynamic therapy · protoporphyrin · singlet oxygen · fluorescence imaging

Despite the progress made during the last few decades, targeted and effective treatment of cancer continues to be a challenge for both clinicians and patients. In this context, photodynamic therapy (PDT) is a promising treatment modality for a variety of oncological conditions. PDT involves the use of a photosensitizer (PS) and laser sources, which are combined to induce cancer cell death.[1−4] In spite of the high potential of this technique over other treatment modalities, PDT faces limitations due to the nonspecific binding of the PS to both healthy and tumor cells, which demands the use of high doses in many cases, increasing the risk of dark toxicity. Another major limitation of currently available sensitizers is the difficulty in the administration and effective delivery to the cancer site due to their low solubility in physiological media. As most of the PSs are nontraceable under conventional imaging techniques, the speculative nature of the accumulation of PS at the cancer site and the subsequent lack of follow-up of therapy limits the practical use of this treatment option. There are several reports on the use of nanoparticles, nanorods, and quantum dots (QDs) for cancer therapy.[5−19] Among them, gold nanoparticle based plasmonic photothermal therapy (PTT) gained much attention in cancer treatment owing to its ability to kill cancerous cells by the local generation of heat. Energy absorbed by the photothermal agents relaxes back to the ground state through the nonradiative decay route, producing local heating. The major limitations of conventional chromophore-based PTT could be overcome by using gold-based nanosystems. A detailed study on the kinetics of cell death using gold nanoprisms by Perez-Hernandez *et al.* suggests that under optimized laser irradiation conditions PTT induces apoptosis in transformed cells by the intrinsic mitochondrial pathway activation, which finally leads to secondary necrosis.[20] However, the major limitation with gold-based nanosystems is their low fluorescence quantum yield to assist fluorescence-imaging-guided cancer treatment.
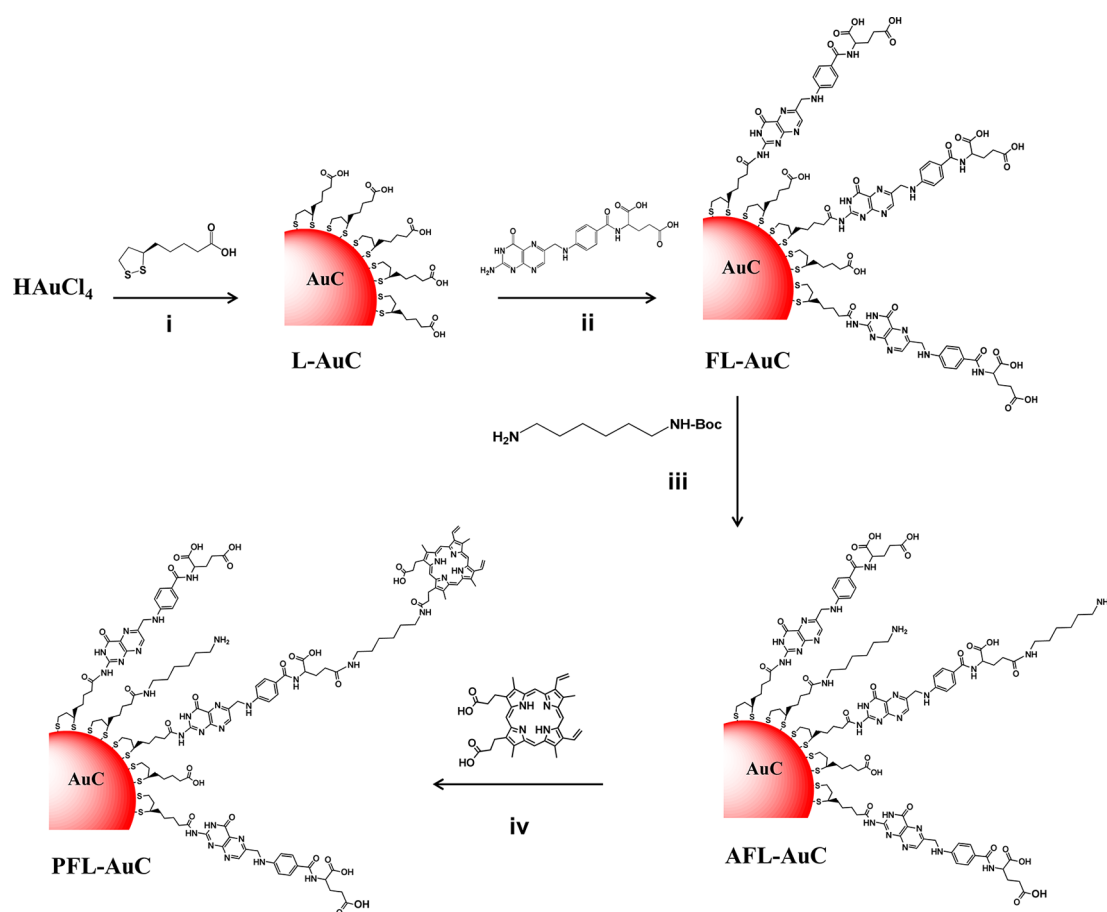
Scheme 1. Synthetic scheme for the preparation of the new imaging/PDT agent. Reagents and conditions: [i] NaOH, NaBH$_4$, 24 h; [ii] EDC/NHS, 12 h; [iii] EDC/NHS, 12 h, TFA/H$_2$O, 3 h; [iv] EDC/NHS, 12 h. All reactions were carried out at 25 °C.

In contrast to PTT, cell death occurs in PDT by the singlet oxygen generated during the relaxation of the excited PS to the triplet state *via* intersystem crossing and subsequent relaxation to the ground state. Therefore, PDT agents, if combined with tumor targeting and a fluorescent imaging agent, will have additional advantages for efficient cancer treatment. Since gold quantum clusters (AuCs)[21−33] have relatively better fluorescent quantum yields when compared to gold nanoparticles, we thought of using the former as a fluorescent immobilizer for the PDT agent and for the tumor-targeting agent. Quantum clusters are composed of very few atoms with a core size of a few nanometers. Clusters of this size range have discrete electronic energy levels unlike their own nanoparticle counterpart, which imparts unique optical properties to these clusters. Recently, Huang *et al.* reported the use of silica-functionalized gold clusters with covalently incorporated chlorin e6 (Ce6) molecules for near-infrared (NIR) fluorescence imaging and PDT.[19] In the context of the above objectives and information available, we have developed a tumor-targeting and NIR-emitting AuC-based multifunctional nanosystem for targeted PDT and fluorescence imaging with sufficiently low doses of PS.

RESULTS AND DISCUSSION

NIR-emitting AuCs capped with lipoic acid (L-AuC) were synthesized according to Scheme 1, which served as the base material for further functionalization to facilitate dual functions of targeted imaging and PDT applications. Quantitative estimation of the lipoic acid groups on AuCs was determined by the MALDI analysis, which gave a loading capacity of 14 molecules per cluster. Subsequently, the L-AuC was reacted with a cancer-targeting moiety, folic acid (FA), using 1-ethyl-3-(3-(dimethylamino)propyl)carbodiimide (EDC) and *N*-hydroxysuccinimide (NHS) coupling agent to get FL-AuC. The number of moles of FA present in FL-AuC was estimated to be approximately 1.67 × 10^{-6}, corresponding to an average of 11 molecules of FA/cluster using UV−vis absorption spectral calibration. A reactive amino group was introduced to FL-AuC by reacting with a Boc-protected hexamethylenediamine (HMDA) derivative followed by the deprotection of the Boc group, resulting in AFL-AuC. Finally, the photosensitizer-linked gold cluster PFL-AuC was prepared by reacting with protoporphyrin IX (PPIX) using EDC/NHS as the coupling agent. The number of HMDA and PPIX molecules per cluster was deliberately kept
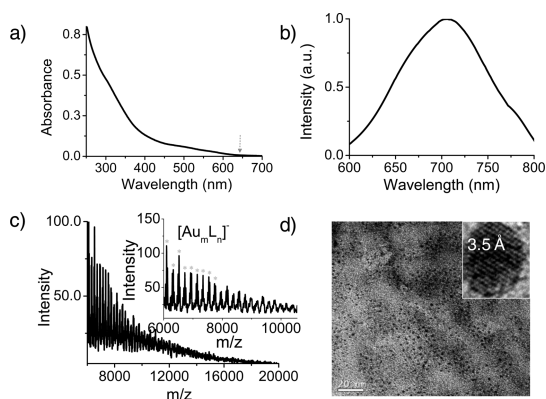
Figure 1. UV−visible absorption spectrum (a), fluorescence emission spectrum upon 460 nm excitation (b), and MALDI MS spectrum (c). Inset shows the expanded mass spectrum of $[Au_{18}L_{14}]^-$ and $[Au_mL_nS]^-$ (m = 19−24; n = 14−16). HRTEM with the lattice spacing (inset) of L-AuC (d).

very low (approximately 1/10th of the FA) in order to make available a sufficient number of free FA for tumor targeting. The number of moles of PPIX on PFL-AuC was estimated to be approximately 1.40×10^{-7} using UV−visible spectroscopy. This value corresponds to an average of one molecule of PPIX in a PFL-AuC cluster.

The UV−vis absorption and emission spectra of the lipoic acid capped gold cluster are shown in Figure 1a and b. From the UV−vis absorption spectra, the optical band gap of L-AuC was estimated as 1.88 eV (660 nm) (Figure 1a), which matches with the reported value for a glutathione-stabilized 18-atom gold cluster.[21,22] L-AuC showed an appreciable emission in the NIR region at around 720 nm for a range of excitation wavelengths from 400 to 550 nm (Figures 1b, S1a). The average particle diameter was *ca*. 1.4 nm (Figure 1d). High-resolution transmission electron microscopy (HR-TEM) analysis revealed a lattice distance of 3.5 Å for this cluster. The X-ray diffraction (XRD) data (Figure S1b) also agrees with this result even though it shows broad peaks, which may be due to the extremely smaller size of the cluster. The observed fluorescence of the cluster is attributed to the intra/interband transition within the conduction band.

Matrix-assisted laser desorption ionization mass spectrometric (MALDI) analysis of L-AuC showed peaks indicative of the simultaneous desorption of gold and sulfur atoms at a laser power of 160 mW (Figure 1c). On the basis of the results of mass spectroscopy and the observed resemblance in the optical band gap, we have assigned the number of Au atoms in a cluster as 18. Subsequently, considering the MALDI-MS peaks and the total mass of L-AuC, the number of ligands present was calculated as 14. The metal−ligand ratio of $(Au)_{18}(L)_{14}$ assigned likewise corresponds to magic number, which imparted the stability to the cluster, justifying the assignment. Further, this assignment was confirmed with the theoretical mass spectrum of the same combination with the help of mass analysis

software (m mass). Theoretical (Figure S1c) and experimental peak fragmentation showed good agreement, justifying the assignment of cluster ligand ratios $(Au)_{18}(L)_{14}$.

The Fourier transform-infrared (FT-IR) spectrum of L-AuC does not show any free S−H peak (Figure S2), indicating the ligation of both S atoms of lipoic acid with the clusters. Since both thiol groups are linked to the Au atoms, we hypothesize that $(Au)_{18}(L)_{14}$ is arranged in such a way that 12 atoms of gold have adopted an icosahedral symmetry utilizing one of the thiol groups of lipoic acid, while the remaining six atoms are connected *via* another thiol group (*i.e.*, the S−Au−S−Au bond). This might be the most plausible way for the system to minimize the potential energy to form a stable cluster system.

Functionalization of L-AuC with folic acid and PS was monitored by the zeta potential analysis and by optical and FT-IR spectroscopy. The negative zeta potential of −36 mV exhibited by L-AuC decreased to −28 mV on conjugation of folic acid (Figure S1d). The UV−vis absorption spectrum of FL-AuC shows a characteristic absorption of folic acid (Figure S3a). The observed shift in the amide bands of FL-AuC in the FT-IR spectrum also supports the functionalization (Figure S2). FL-AuC shows red edge excitation emission, a phenomenon where the emission peak red shifts as the excitation increases.[34,35] This phenomenon was observed initially in the case of folic acid at basic pH and later in FL-AuC. Red edge excitation occurs due to the change in dipole moment of the folic acid and the rate of reorientation of the water molecules as a result of a change in the FA−water interaction in the ground and excited states. This difference in excitation is also maintained in the fluorescence lifetime of FL-AuC, which showed a lifetime of 37 ms when compared to the 401 ns of L-AuC (Figures S4b, S5a). Also, in the case of FL-AuC, an increase in the intensity of the 720 nm emission peak was observed, which may be attributed to the fluorescence resonance energy transfer (FRET) between L-AuC and the folic acid ligand. The origin of FRET is due to the overlapping of the emission of FA, which is bound to the lipoic acid with the excitation of L-AuC.

The presence of folic acid and PPIX in PFL-AuC was evident from the absorption spectrum (Figure S3b). The negative zeta potential of −28 mV of FL-AuC further decreased on addition of HMDA (*ca*. −19 mV) and then increased to −25 mV on addition of PPIX, indicating the changes in the functionality on the surface of L-AuC at different stages of functionalization (Figure S1b). Again, the shift observed in the amide peaks in the FT-IR spectrum of PFL-AuC is indicative of the attachment of PPIX. The emission spectrum of PFL-AuC showed the characteristic emission peaks of folic acid, PPIX, and L-AuC, confirming the presence of these components in the final system. The particle size of FL-AuC and PFL-AuC remains the same as that of L-AuC, as

is evident from the TEM images (Figure S5c,d). The fluorescence quantum yield estimated for FL-AuC (Figure S4a) was 10%, which was reduced to 5.1% in PFL-AuC on conjugation with PPIX. The fluorescence lifetime (Figures S4b, S5a,b) of PFL-AuC decreased to 5.68 ps from 37 ms of FL-AuC. The decrease in the fluorescence quantum yield of PFL-AuC at 720 nm is due to the increase in the distance between PPIX and the core atom.

In order to use the developed system as a photosensitizer for photodynamic therapy, the singlet oxygen generation efficiency of PFL-AuC was determined by the direct spectroscopic observation of singlet oxygen emission at 1270 nm by 530 nm excitation (Figure 2a). The singlet oxygen production was reconfirmed by monitoring the time-dependent depletion of the absorption of diphenylisobenzofuran (DPBF) at 398 nm (Figures 2b, S6).[28] The singlet oxygen yield of PFL-AuC was 80% when compared to 63% of PPIX (Figure S6). The high singlet oxygen efficiency with low loading of PPIX makes PFL-AuC an efficient PDT agent with imaging capability. Moreover, the presence of a sufficient number of cancer cell targeting agents in PFL-AuC helps the local generation of the singlet oxygen in the tumor cells even with a low loading of PPIX, leaving the normal cells unaffected.
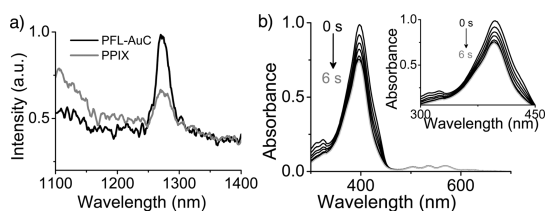

Figure 2. Singlet oxygen generation of PFL-AuC and PPIX as observed by the phosphorescence of singlet oxygen at 1270 nm upon excitation by a 530 nm laser (a) and the same detected by the time-dependent decrease in the absorption of DPBF (b). Inset shows the expanded spectral profile.

The nontoxicity of the developed system was confirmed with L929 mouse fibroblasts by checking the cytocompatibility of the developed nanocarrier by the activity of mitochondrial reductase using the MTT assay (Figure S7). The feasibility of the developed material for *in vitro* imaging and PDT was checked with a folate-overexpressed cancer cell line (C6 rat glial cells). The targeting efficacy of the material was studied after incubating with 1 mg/mL (1.55×10^{-4} M) of L-AuC, FL-AuC, and PFL-AuC (Figure 3, Figure S8), using fluorescence microscopy. Furthermore, the cellular uptake efficacy of the developed probe was quantified using inductively coupled plasma mass spectrometry (ICP-MS) analysis (Figure S9), which revealed uptakes of 89, 46, and 26 ppm of gold when cells were treated with 1.55×10^{-4}, 7.78×10^{-5}, and 1.55×10^{-5} M concentrations of PFL-AuC. PDT efficiency of PFL-AuC was assessed by irradiating the cells with a 532 nm laser (1.5 W/cm^2) for 30 s. A batch of cells without PFL-AuC under laser irradiation at the same dosage and another batch of cells in the presence of PFL-AuC without laser irradiation served as controls (Figure 3e). As seen from Figure 3d and e, cell death is negligible in the case of control cells after 30 s of laser irradiation, whereas significant cell death was observed in the cells carrying PFL-AuC. Cells incubated with PFL-AuC that did not receive laser treatment (Figure 3d) also showed no cell death.

Concentration-dependent PDT efficacy of PFL-AuC was demonstrated by measuring the cell viability on addition of both PPIX and PFL-AuC before (Figure S10a) and after (Figure S10b) laser irradiation. Percentage viability was assessed using MTT with different concentrations [80 μg (1.8×10^{-4} M), 60 μg (1.36×10^{-4} M), 40 μg (9.07×10^{-5} M), 20 μg (4.53×10^{-5} M), 10 μg (2.26×10^{-5} M), 8 μg (1.81×10^{-5} M), and 5 μg (1.13×10^{-5} M)] of PPIX and PFL-AuC. The IC$_{50}$ value of PFL-AuC is 60 μg (1.36×10^{-4} M), whereas the same concentration of PPIX alone shows more than 70% cell
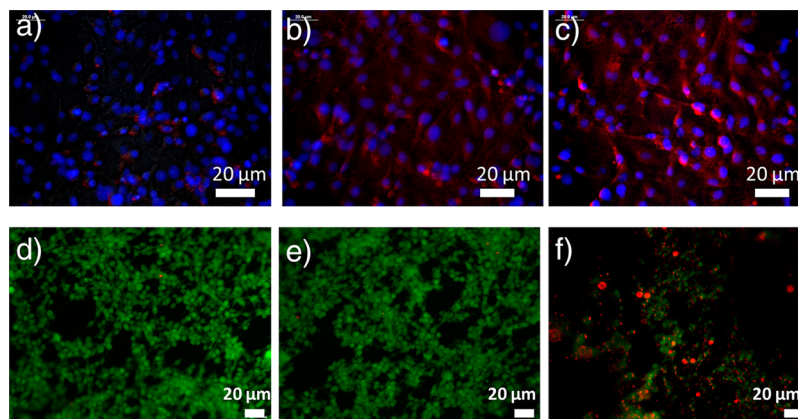

Figure 3. *In vitro* fluorescence images of L-AuC (a), FL-AuC (b), and PFL-AuC (c). Fluorescence from the cluster is red, and the Hoechst-stained nucleus is blue. Live dead assay of cells (d to f): cells with laser irradiation alone (d), cells with PFL-AuC, without laser irradiation (e), cells with PFL-AuC with laser irradiation showing maximum cell death (f). Green color represents live cells, and red color represents dead cells.
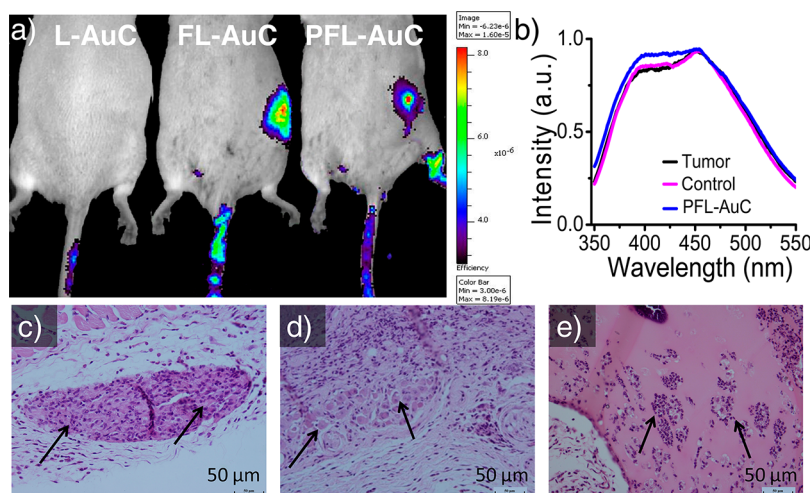
Figure 4. *In vivo* targeted tumor imaging (a). Autofluorescence spectra at 320 nm excitation as a measure of collagen variation (b). H&E stained sections (c—e): control animals showing tumor infiltration with dividing cells (c), tumor treated with laser alone showing dividing cells (d), and tumor treated with PFL-AuC and laser showing necrotic cells (e).

viability (Figure S10). Less uptake of PPIX by the cells accounts for this observation (Figure S11). Cells incubated with PFL-AuC without laser irradiation showed comparatively less cell death (Figure S10a).

To demonstrate *in vivo* tumor-targeting efficacy, imaging, and therapeutic potential, the newly developed nanoclusters were injected intravenously into mouse models of subcutaneous C6 glial tumor. Animals with well-defined tumor margins were selected for this purpose (Figure S12). On imaging under a live animal optical imaging system (Xenogen, IVIS Spectrum), L-AuC-injected animals showed no signal output from the tumor when compared to the FL-AuC- and PFL-AuC-injected animals (Figure 4a). For the *in vivo* imaging of tumor, 640 nm excitation was used to avoid interference from the first biological window and get maximum signal from the material. Appreciable absorbance of PFL-AuC around 640 nm and the corresponding NIR emission upon excitation at 640 nm (Figure S13) favored the selection of this excitation wavelength for *in vivo* studies. Less quantum yield and the absence of the tumor-targeting folate moiety of L-AuC when compared to PFL-AuC account for the absence of signal from the control. Tumor-targeting efficiency of PFL-AuC facilitated the accumulation of the material in the tumor, which enhanced the signal from the site, enabling *in vivo* imaging of the tumor and also the PDT follow-up. An *ex vivo* distribution of the developed probe shows maximum uptake in the tumor site (Figure S14). A detailed biodistribution of the probe at 3 and 24 h after injection was carried out in C6 tumor-induced mice. It is clear from this study that after 3 h of injection the majority of the PFL-AuC is accumulated in the tumor region (Figure S15). However, after 24 h, 43% reduction of the concentration of PFL-AuC from the tumor site and an increase of more than double the concentration are seen in the liver and kidney (Figure S15).

In order to demonstrate the PDT efficacy of PFL-AuC, the animals were irradiated with a 532 nm laser (1.5 W/cm^2) for 15 min after 3 h of intravenous injection of the new materials. Tumor-bearing animals irradiated with a laser served as a control. The effect of treatment was monitored up to the seventh day of laser irradiation by measuring the changes in tumor volume. The therapeutic efficacy was also assessed by monitoring the tumor markers such as collagen (Figure 4b), total hemoglobin concentration, and redox ratio (Figure S16). This was achieved by measuring the emission spectra of endogenous fluorophores from the tumor site, using fiber-optic fluorescence spectroscopy.[36—39] Tumor volume reduction was observed in the PFL-AuC group up to the fifth day and remained unchanged thereafter (Figure S16a). However, the tumor markers showed considerable change until the seventh day, when collagen level, redox ratio, and total hemoglobin concentration of the PFL-AuC-treated animals were almost equal to those of normal animals. Noticeably, there was a considerable increase in the tumor volume among the control animals up to 7 days. On resuming normal condition, animals were sacrificed on the seventh day to reconfirm tumor development and treatment efficacy, histopathologically (Figure 4d,e).

CONCLUSION

To summarize, we have developed a biocompatible gold cluster based multifunctional nanosystem for fluorescence-imaging-directed PDT applications. Even though the fluorescence quantum yield of the L-AuC is relatively low when compared to that of semiconductor quantum dots or organic fluorophores, the localization of the clusters on tumor cells allowed fluorescence imaging with reasonably good intensity, as shown in Figure 3. Singlet oxygen efficiency of PFL-AuC is found to be significantly high

when compared to that of the PPIX alone. The enhanced singlet oxygen generation with low loading of PPIX and the better localization of the PFL-AuC on tumor cells facilitated targeted cell death with a sufficiently low dose of laser irradiation. Moreover, the NIR emission of PFL-AuC facilitates real-time tracking of the progress of PDT. An *in vivo* study with animal models shows that the developed nanocluster is useful for the effective destruction and monitoring of tumor cells. The future prospect of the described system is to use it as a suitable therapeutic agent for clinical practice.

MATERIALS AND METHODS

Materials Used. Chloroauric acid (HAuCl₄), lipoic acid (LA), hexamethylenediamine (HMDA), folic acid (FA), 1-ethyl-3-(3-(dimethylamino)propyl)carbodiimide (EDC), N-hydroxysuccinimide (NHS), protoporphyrin IX (PPIX), calcein propedium iodide, and Hoescht were purchased from Sigma, Bangalore, India. Sodium borohydride (NaBH₄), sodium hydroxide (NaOH), and hydrochloric acid (HCl) were obtained from Merck India Pvt. Ltd. Modified Eagle medium (MEM), Hams F12 medium, fetal bovine serum (FBS), and trypsin were obtained from Himedia. All chemicals were used as such without any further purification unless stated otherwise. All glassware was cleaned using *aqua regia* (1:3 ratio of HCl and HNO₃). The water used in all experiments was Millipore Milli Q grade (18 MΩ·cm).

Synthesis of Lipoic Acid Capped Gold Cluster (L-AuC). A 2.4 mg amount of LA (1.5 mM) was dissolved in 8 mL of deionized (DI) water, and the solution stirred at room temperature (25 °C). To this was added 40 μL of NaOH (1 M), and the solution stirred for 30 min, followed by the dropwise addition of 80 μL of HAuCl₄ (50 mM), and incubated for 15 min. When the solution became colorless, 160 μL of 50 mM ice-cold NaBH₄ was added. After 24 h the solution became bright yellow in color. This solution was centrifuged at 15000 rpm for 15 min in a 1:1 methanol/2-propanol mixture and lyophilized to get L-AuC, which was used for further study.

Preparation of Folic Acid Functionalized L-AuC (FL-AuC). L-AuC (2 mg) was dispersed in 5 mL of DI water. A 0.25 mL amount of EDC (0.05 M) in water was added, and the pH was adjusted to 4, and the mixture was stirred for 2 h. Subsequently, 0.25 mL of NHS (0.05 M) in water was added followed by the addition of folic acid (4 mM, 2 mL) under basic pH. The pH of the solution was then adjusted to 9, and the reaction was continued for another 12 h. The reaction mixture was centrifuged at 15 000 rpm for 15 min in a 1:1 methanol/2-propanol mixture and washed twice with DI water to obtain FL-AuC.

Preparation of the Protoporphyrin IX (PPIX)-Linked Gold Cluster PFL-AuC. FL-AuC (2 mg) was dispersed in 5 mL of DI water. A 0.326 mg portion of Boc-protected HMDA in methanol, EDC (0.25 mL, 0.05 M), and NHS (0.25 mL, 0.05 M) were added. After 12 h, HMDA-conjugated FL-AuC was separated by centrifuging at 15 000 rpm for 15 min in a 1:1 methanol/2-propanol mixture. This was treated with trifluoroacetic acid (TFA) and water (1:1, 5 mL) and stirred for 3 h, and the solution was centrifuged at 15 000 rpm for 15 min in a 1:1 methanol/2-propanol mixture. The resulting product, AFL-AuC, was resuspended in DI water. A 2 mg sample of AFL-AuC dispersed in 5 mL of DI water was added to EDC/NHS (as mentioned before)-activated PPIX (1 mg in 0.001 N NaOH). The reaction was continued for 12 h, followed by centrifugation at 15 000 rpm for 15 min in a 1:1 methanol/2-propanol mixture, washed with water twice, dried, and used for further study.

Description of Experimental Techniques. Details of the UV−vis−NIR absorption and emission spectra, FT-IR spectra, zeta potential measurements, and the estimation of the number of ligands are given in the Supporting Information.

Matrix-Assisted Laser Deposition Ionization Mass Spectroscopy. MALDI spectra of the gold clusters were recorded using a Shimadzu KRATOS analytical AXIMA-CFR Plus. A 20 μL amount of L-AuC dispersed in a 1:1 water/methanol mixture was used for the analysis. An α-cyano-4-hydroxycinnamic acid matrix was used, and the spectrum was recorded from 2000 to 20 000 at 160 mW laser power.

High-Resolution Transmission Electron Microscopy. HR-TEM images of the samples were recorded using an FEI, TECNAI 30 G2 S-TWIN microscope at an accelerating voltage of 300 kV. Diluted samples were drop-casted on a Formvar-coated copper grid and dried at room temperature.

Fluorescence Lifetime Measurements. Fluorescence lifetimes of the newly prepared gold clusters were measured using an IBH (FluoroCube) time-correlated picosecond single photon counting (TCSPC) system. Solutions were excited with a pulsed diode laser (<100 ps pulse duration) at a wavelength of 440 nm (NanoLED-10) with a repetition rate of 1 MHz. The detection system consists of a microchannel plate photomultiplier (5000U-09B, Hamamatsu) with a 38.6 ps response time coupled to a monochromator (5000M) and TCSPC electronics (DataStation Hub including Hub-NL, NanoLED controller, and preinstalled Fluorescence Measurement and Analysis Studio (FMAS) software). The fluorescence lifetime values were determined by deconvoluting the instrument response function with biexponential decay using DAS6 decay analysis software.

Determination of Singlet Oxygen Quantum Yield. Singlet-oxygen-generation studies were performed with a 200 W mercury lamp as light source on an Oriel optical bench with a grating monochromator. The intensity of the light was kept constant throughout the irradiations by measuring the output with an Oriel photodiode detection system. Quantum yields of the singlet oxygen generation were measured by dispersing PFL-AuC and PPIX in methanol. Absorbance of both the materials was kept at 530 nm, since the excitation filter used was 530 nm. A 10 μL amount of 1,3-diphenylisobenzofuran was added to both PFL-AuC and PPIX, and the decrease in intensity upon irradiation with 530 nm light was monitored. The decrease in absorbance was monitored from 0 to 6 s for both PFL-AuC and PPIX.

Cellular Uptake and Targeted PDT *in Vitro*. C6 rat glial cells were obtained from NCCS, Pune, India. C6 cells were cultured with a 1:1 ratio of MEM and F12 Ham media containing 10% FBS in 5% CO_2 at 37 °C. Cellular uptake and PDT efficacy of the nanomaterials were checked. The developed probes were dissolved in phosphate-buffered saline having pH 7.4. For cellular uptake, to the confluent cell monolayer was added 1 mg/mL of the materials, and the mixture was incubated for 3 h. The cells were then washed with phosphate-buffered saline (PBS) and stained with Hoescht. The uptake efficacy was checked using a fluorescence microscope. For targeted cellular PDT, after 3 h of incubation of PFL-AuC in a monolayer of cells, a 532 nm laser (0.5 W/cm²) was irradiated for 30 s. After 15 min, the cells were stained with calcein propedium iodide, and the live and dead cells were assessed using a fluorescence microscope.

Quantification of PFL-AuC *in Vitro* Using ICP-MS. ICP-MS analysis was conducted using an ICAP Q_c (Thermo Scientific) with a plasma power of 1550 W. Plasma, nebulizer, and auxiliary flow rate are 14, 0.97, and 0.80 L/min, respectively. C6 cells were cultured in a T 25 flask. The confluent cell monolayer was incubated with three different concentrations (1.55×10^{-4}, 7.78×10^{-5}, and 1.55×10^{-5} M) of PFL-AuC for 3 h. The cells were washed three times with PBS. Cells were trypsinized, and the cell pellets were again washed three times with PBS. Wet weights of the cell pellets were noted. Cells were digested using 300 μL of HNO₃ and 8 mL of *aqua regia* using a multiwave reaction system (Multiwave 3000, Anton Paar). Digested cell samples were diluted to a known volume using Milli-Q water. Au content present in the unknown samples was analyzed by ICP-MS from the calibration plot of a known Au standard.

Tumor Imaging and PDT *in Vivo*. The tumor model was developed in mice by injecting 150 μL of the C6 cell line in Matrigel (BD Biosciences) subcutaneously. When the tumor volume reached around 0.7 cm^3, 0.5 mL (1 mg/mL) of nanoparticles was injected through the tail vein (iv). Tumor imaging was done using a Xenogen IVIS Spectrum optical imaging system after 3 h of injection.

For tumor imaging, Albino Swiss mice with a normal body weight of 30−50 g were anesthetized using xylazine and ketamine. The dorsal side of the animals was clipped to remove the hair. A sterile formulation of 1 mg/mL of nanomaterials in 1× PBS having pH 7.3 was injected intravenously into the anesthetized animals through the tail vein. Live animal imaging was performed using the Xenogen IVIS Spectrum optical imaging system at different excitation and emission wavelengths.

For targeted PDT, PFL-AuC (in 1× PBS) was injected intravenously into the tumor-bearing animals. After 3 h of injection, the tumor site was irradiated with a 532 nm laser for 15 min (1.5 W/cm^2). Tumor-bearing mice without gold clusters, but irradiated with the same laser, served as the control. Tumor volume was monitored daily using vernier calipers. In addition, tumor regression was also monitored by assessing the markers collagen, FAD, and NADH[37] using a fiber-optic accessory of a spectrofluorimeter (Jobin Yvon) by exciting at 320 nm. A ratiometric evaluation of the total hemoglobin concentration[36−39] based on the spectral filtering modulation effect of hemoglobin is observed in the fluorescence spectrum (at 410 nm excitation) and is calculated using the equation

$$\text{Total hemoglobin concentration } (C_{Hb}) = FI_{500}/FI_{570}$$

This ratio is directly correlated to the total hemoglobin concentration, which is considered an important cancer biomarker. An increased hemoglobin concentration is an indication of increased angiogenesis (new vasculature) typical of tumor conditions.

Additionally, monitoring the redox ratio (at 320 nm excitation) is one of the most common ways of assessing metabolic activity. This optical redox ratio provides relative changes in the oxidation−reduction state in the cell. The redox ratio is sensitive to changes in the metabolic activity and vascular oxygen supply. Due to the increase in the metabolic activity in the tumor, the redox ratio increases.

$$\text{Redox ratio} = FAD_{intensity}/FAD_{intensity} + NADH_{intensity}$$

where $FAD_{intensity}$ and $NADH_{intensity}$ are the emission intensities at 530 and 460 nm, respectively.

Histopathological Evaluation. On the seventh day, the animals were sacrificed and the tissue sections were fixed in formalin. The formalin-fixed tissue sections were processed by various stages of dehydration after 2 weeks. After dehydration, the tissues were embedded in paraffin cassettes. Tissues were sectioned to slices of 0.4 μm thickness using a microtome. Sections were fixed on glass slides and dried under ambient conditions. These tissue sections were subjected to different concentrations of xylene and alcohol for hematoxylene and eosin staining. The H&E-stained sections were viewed under a microscope to assess the tumor growth and regression in the control and treated groups, respectively.

Conflict of Interest: The authors declare no competing financial interest.

Supporting Information Available: XRD, zeta potential, theoretical mass spectra of L-AuC, FT-IR spectra of L-AuC, FL-AuC, and PFL-AuC, absorption and emission spectra of FL-AuC and PFL-AuC, quantum yield, fluorescence lifetimes of L-AuC, FL-AuC, and PFL-AuC, TEM images of FL-AuC and PFL-AuC, singlet oxygen generation of protoporphyrin IX, MTT assay of L-AuC, FL-AuC, and PFL-AuC, bright-field images of L-AuC, FL-AuC, and PFL-AuC treated cells, ICP-MS analysis of PFL-AuC in cells, percentage cell viability of PFL-AuC and PPIX before and after laser irradiation, cellular uptake study of PPIX in C6 glial cells, absorption spectrum of PFL-AuC from 600 to 700 nm and its corresponding emission at 640 nm excitation, photographs of tumor-bearing mice, *ex vivo* distribution of nanoparticles, detailed biodistribution of PFL-AuC in tumor-induced mice for

3 and 24 h, *in vivo* tumor evaluation of PDT. The Supporting Information is available free of charge on the ACS Publications website at DOI: 10.1021/acsnano.5b00406.

REFERENCES AND NOTES

1. Castano, A. P.; Mroz, P.; Hamblin, M. R. Photodynamic Therapy and Anti-Tumour Immunity. *Nat. Rev. Cancer* **2006**, *6*, 535–545.

2. Chatterjee, D. K.; Fong, L. S.; Zhang, Y. Nanoparticles in Photodynamic Therapy: An Emerging Paradigm. *Adv. Drug Delivery Rev.* **2008**, *60*, 1627–1637.

3. Lovell, J. F.; Liu, T. W. B.; Chen, J.; Zheng, G. Activatable Photosensitizers for Imaging and Therapy. *Chem. Rev.* **2010**, *110*, 2839–2857.

4. Celli, J. P.; Spring, B. Q.; Rizvi, I.; Evans, C. L.; Samkoe, K. S.; Verma, S.; Pogue, B. W.; Hasan, T. Imaging and Photodynamic Therapy: Mechanisms, Monitoring, and Optimization. *Chem. Rev.* **2010**, *110*, 2795–2838.

5. Jain, P. K.; Huang, X.; El-Sayed, I. H.; El-Sayed, M. A. Review of Some Interesting Surface Plasmon Resonance-enhanced Properties of Noble Metal Nanoparticles and Their Applications to Biosystems. *Plasmonics* **2007**, *2*, 107–118.

6. Maji, S. K.; Sreejith, S.; Mandal, A. K.; Ma, X.; Zhao, Y. Immobilizing Gold Nanoparticles in Mesoporous Silica Covered Reduced Graphene Oxide: A Hybrid Material for Cancer Cell Detection through Hydrogen Peroxide Sensing. *ACS Appl. Mater. Interfaces* **2014**, *6*, 13648–13656.

7. Komatsu, H.; Shindo, Y.; Oka, K.; Hill, J. P.; Ariga, K. Ubiquinone-Rhodol (UQ-Rh) for Fluorescence Imaging of NAD-(P)H through Intracellular Activation. *Angew. Chem., Int. Ed.* **2014**, *53*, 3993–3995.

8. Akamatsu, M.; Komatsu, H.; Mori, T.; Adams, E.; Shin, R.; Sakai, H.; Abe, M.; Hill, J. P.; Ariga, K. Intracellular Imaging of Cesium Distribution in *Arabidopsis* Using Cesium Green. *ACS Appl. Mater. Interfaces* **2014**, *6*, 8208–8211.

9. Ipe, B. I.; Yoosaf, K.; Thomas, K. G. Functionalized Gold Nanoparticles as Phosphorescent Nanomaterials and Sensors. *J. Am. Chem. Soc.* **2006**, *128*, 1907–1913.

10. Biju, V. Chemical Modifications and Bioconjugate Reactions of Nanomaterials for Sensing, Imaging, Drug Delivery and Therapy. *Chem. Soc. Rev.* **2014**, *43*, 744–764.

11. Kalluru, P.; Vankayala, R.; Chiang, C.; Hwang, K. Photosensitization of Singlet Oxygen and *in Vivo* Photodynamic Therapeutic Effects Mediated by PEGylated $W_{18}O_{49}$ Nanowires. *Angew. Chem., Int. Ed.* **2013**, *52*, 12332–12336.

12. Nair, L. V.; Nagaoka, Y.; Maekawa, T.; Sakthikumar, D.; Jayasree, R. S. Quantum Dot Tailored to Single Wall Carbon Nanotubes: A Multifunctional Hybrid Nanoconstruct for Cellular Imaging and Targeted Photothermal Therapy. *Small* **2014**, *10*, 2771–2775.

13. Zhan, N.; Palui, G.; Safi, M.; Mattoussi, H. Multidentate Zwitterionic Ligands Provide Compact and Highly Biocompatible Quantum Dots. *J. Am. Chem. Soc.* **2013**, *135*, 13786–13795.

14. Huang, X.; El-Sayed, I. H.; Qian, W.; El-Sayed, M. A. Cancer Cell Imaging and Photothermal Therapy in the Near-Infrared Region by Using Gold Nanorods. *J. Am. Chem. Soc.* **2006**, *128*, 2115–2120.

15. Dickerson, E. B.; Dreaden, E. C.; Huang, X.; El-Sayed, I. H.; Chu, H.; Pushpanketh, S.; McDonald, J. F.; El-Sayed, M. A. Gold Nanorod Assisted Near-Infrared Plasmonic Photothermal Therapy (PPTT) of Squamous Cell Carcinoma in Mice. *Cancer Lett.* **2008**, *269*, 57–66.

16. Zhao, T.; Wu, H.; Yao, S. Q.; Xu, Q. H.; Xu, G. Q. Nanocomposites Containing Gold Nanorods and Porphyrin-Doped

Mesoporous Silica with Dual Capability of Two-Photon Imaging and Photosensitization. *Langmuir* **2010**, *26*, 14937–14942.

17. Eshghi, H.; Sazgarnia, A.; Rahimizadeh, M.; Attaran, N.; Bakavoli, M.; Soudmand, S. Protoporphyrin IX—Gold Nanoparticle Conjugates as an Efficient Photosensitizer in Cervical Cancer Therapy. *Photodiagn. Photodyn. Ther.* **2013**, *10*, 304–312.

18. Cheng, L.; Wang, C.; Feng, L.; Yang, K.; Liu, Z. Functional Nanomaterials for Phototherapies of Cancer. *Chem. Rev.* **2014**, *114*, 10869–10939.

19. Huang, P.; Lin, J.; Wang, S.; Zhou, Z.; Li, Z.; Wang, Z.; Zhang, C.; Yue, X.; Niu, G.; Yang, M.; *et al*. Photosensitizer-Conjugated Silica-Coated Gold Nanoclusters for Fluorescence Imaging-Guided Photodynamic Therapy. *Biomaterials* **2013**, *34*, 4643–4654.

20. Pérez-Hernández, M.; Del Pino, P.; Mitchell, S. G.; Moros, M.; Stepien, G.; Pelaz, B.; Parak, W. J.; Gálvez, E. M.; Pardo, J.; de la Fuente, J. M. Dissecting the Molecular Mechanism of Apoptosis during Photothermal Therapy Using Gold Nanoprisms. *ACS Nano* **2015**, *9*, 52–61.

21. Negishi, Y.; Takasugi, Y.; Sato, S.; Yao, H.; Kimura, K.; Tsukuda, T. Magic-Numbered Au$_n$ Clusters Protected by Glutathione Monolayers (n = 18, 21, 25, 28, 32, 39): Isolation and Spectroscopic Characterization. *J. Am. Chem. Soc.* **2004**, *126*, 6518–6519.

22. Negishi, Y.; Nobusada, K.; Tsukuda, T. Glutathione-Protected Gold Clusters Revisited: The Bridging the Gap between Gold(I)—Thiolate Complexes and Thiolate-Protected Gold Nanocrystals. *J. Am. Chem. Soc.* **2005**, *127*, 5261–5270.

23. Xavier, P. L.; Chaudhari, K.; Baksi, A.; Pradeep, T. Protein-Protected Luminescent Noble Metal Quantum Clusters: An Emerging Trend in Atomic Cluster Nanoscience. *Nano Rev.* **2012**, *3*, 14767.

24. Muhammed, M. A. H.; Ramesh, S.; Sinha, S. S.; Pal, S. K.; Pradeep, T. Two Distinct Fluorescent Quantum Clusters of Gold Starting from Metallic Nanoparticles by pH-Dependent Ligand Etching. *Nano Res.* **2008**, *1*, 333–340.

25. Lin, C. A. J.; Yang, T.; Lee, C.; Huang, S. H.; Sperling, R. A.; Zanella, M.; Li, J. K.; Shen, J. L.; Wang, H. H.; Yeh, H. I.; *et al*. Synthesis, Characterization, and Bioconjugation of Fluorescent Gold Nanoclusters toward Biological Labeling Applications. *ACS Nano* **2009**, *3*, 395–401.

26. Shang, Li.; Azadfar, N.; Stockmar, F.; Send, W.; Trouillet, V.; Bruns, M.; Gerthsen, D.; Ulrich Nienhaus, G. One-Pot Synthesis of Near-Infrared Fluorescent Gold Clusters for Cellular Fluorescence Lifetime Imaging. *Small* **2011**, *7*, 2614–2620.

27. Aldeek, F.; Muhammed, M. A. H.; Palui, G.; Zhan, N.; Mattoussi, H. Growth of Highly Fluorescent Polyethylene Glycol- and Zwitterion-Functionalized Gold Nanoclusters. *ACS Nano* **2013**, *7*, 2509–2521.

28. Cui, S.; Yin, D.; Chen, Y.; Di, Y.; Chen, H.; Ma, Y.; Achilefu, S.; Gu, Y. *In Vivo* Targeted Deep-Tissue Photodynamic Therapy Based on Near-Infrared Light Triggered Upconversion Nanoconstruct. *ACS Nano* **2013**, *7*, 676–688.

29. Pan, L.; Liu, J.; Shi, J. Intranuclear Photosensitizer Delivery and Photosensitization for Enhanced Photodynamic Therapy with Ultralow Irradiance. *Adv. Funct. Mater.* **2014**, *24*, 7318–7327.

30. Medintz, I. L.; Uyeda, H. T.; Goldman, E. R.; Mattoussi, H. Quantum Dot Bioconjugates for Imaging, Labelling and Sensing. *Nat. Mater.* **2005**, *4*, 435–446.

31. Gu, W.; Larabel, C.; Alivisatos, A. P. Quantum Dots as Cellular Probes. *Annu. Rev. Biomed. Eng.* **2005**, *7*, 55–76.

32. Aldeek, F.; Ji, X.; Mattoussi, H. Quenching of Quantum Dot Emission by Fluorescent Gold Clusters: What It Does and Does Not Share with the Förster Formalism. *J. Phys. Chem. C* **2013**, *117*, 15429–15437.

33. Nair, L. V.; Philip, D. S.; Jayasree, R. S.; Ajayaghosh, A. A Near-Infrared Fluorescent Nanosensor (AuC@Urease) for the Selective Detection of Blood Urea. *Small* **2013**, *9*, 2673–2677.

34. Chattopadhyay, A.; Mukherjee, S. Red Edge Excitation Shift of a Deeply Embedded Membrane Probe: Implications in Water Penetration in the Bilayer. *J. Phys. Chem. B* **1999**, *103*, 8180–8185.

35. Weber, G.; Shinitzky, M. Failure of Energy Transfer between Identical Aromatic Molecules on Excitation at the Long Wave Edge of the Absorption Spectrum. *Proc. Natl. Acad. Sci. U.S.A.* **1970**, *65*, 823–830.

36. Nazeer, S. S.; Saraswathy, A.; Gupta, A. K.; Jayasree, R. S. Fluorescence Spectroscopy as a Highly Potential Single-Entity Tool to Identify Chromophores and Fluorophores: Study on Neoplastic Human Brain Lesions. *J. Biomed. Opt.* **2013**, *18*, 067002.

37. Nazeer, S. S.; Saraswathy, A.; Gupta, A. K.; Jayasree, R. S. Fluorescence spectroscopy to Discriminate Neoplastic Human Brain Lesions: A Study Using the Spectral Intensity Ratio and Multivariate Linear Discriminant Analysis. *Laser Phys.* **2014**, *24*, 025602.

38. Skala, M. C.; Riching, K. M.; Gendron-Fitzpatrick, A.; Eickhoff, J.; Eliceiri, K. W.; White, J. G.; Ramanujam, N. *In Vivo* Multiphoton Microscopy of NADH and FAD Redox States, Fluorescence Lifetimes, and Cellular Morphology in Precancerous Epithelia. *Proc. Natl. Acad. Sci. U.S.A.* **2007**, *104*, 19494–19499.

39. Liu, Q.; Vo-Dinh, T. Spectral Filtering Modulation Method for Estimation of Hemoglobin Concentration and Oxygenation Based on a Single Fluorescence Emission Spectrum in Tissue Phantoms. *Med. Phys.* **2009**, *36*, 4819–4829.